ICARUS 53, 236–254 (1983)

Micron-Sized Particles Detected near Saturn by the Voyager Plasma Wave Instrument[1]

D. A. GURNETT,* E. GRÜN,† D. GALLAGHER,*
W. S. KURTH,* AND F. L. SCARF‡

*Department of Physics and Astronomy, The University of Iowa, Iowa City, Iowa 52242, †Max-Planck-Institut für Kernphysik, Postfach 103980, 6900 Heidelberg, West Germany, and ‡Space Science Department, TRW Defense and Space Systems Group, Redondo Beach, California 90278

Received July 6, 1982; revised October 14, 1982

During the Voyager 2 Saturn encounter the plasma wave instrument detected a region of intense impulsive noise centered on the ring plane at a distance of 2.88 Saturn radii, slightly outside of the G ring. The noise has been attributed to small micron-sized particles hitting the spacecraft. Investigation of various coupling mechanisms suggested that the noise was produced by impact ionization of particles striking the spacecraft body, thereby releasing a cloud of charged particles, some of which were collected by the plasma wave antenna. Reasonably reliable estimates of the charge yield per unit mass are available from laboratory impact ionization measurements. Based on the assumption that the voltage induced on the antenna is proportional to the mass of the colliding particle, a method was developed to determine the mass and size distribution of the particles from the rms voltage of the induced noise and the impulse rate. The results obtained show that the mass distribution varies as m^{-3}, and that most of the particles detected had radii in the range from 0.3 to 3 μm. The effective north–south thickness of the particle distribution is 106 km. The mass distribution function derived from these data is shown to be in reasonable agreement with optical depth estimates obtained from imaging measurements and absorption effects detected by energetic charged particle measurements.

I. INTRODUCTION

During the Voyager 2 flyby of Saturn, a region of very intense impulsive noise was detected by the plasma wave and radio astronomy instruments as the spacecraft crossed the ring plane at a radial distance of 2.88 R_S, slightly beyond the G ring (Scarf *et al.*, 1982; Warwick *et al.*, 1982). Because the spectrum of this noise extended upward to frequencies well above the local electron plasma frequency it was concluded that this noise could not be due to plasma waves. The impulsive character of the noise and the close proximity to the ring plane led to the conclusion that the noise was produced by impacts of particles hitting the spacecraft. The basic picture which has evolved is that the noise is produced by many very small, micrometer-sized dust particles probably associated with the outer regions of the G ring. Because of the very large relative velocity of about 14 km/sec between the spacecraft and the particles, a particle hitting the spacecraft is instantly vaporized, producing a small partially ionized cloud of gas that expands outward from the point of impact. Some of the charge in this cloud is collected by the plasma wave and radio astronomy antennas, thereby producing the electrical noise spectrum detected by these instruments.

In this paper we present a detailed study of these impact effects. The objectives are, first, to provide a detailed description of the observational characteristics of the impact-generated noise; second, to discuss the mechanisms involved in the coupling of the

[1] Paper presented at the "Saturn Conference," Tucson, Arizona, May 11–15, 1982.

0019-1035/83 $3.00

impacts to the electric antenna; and third, to use the observed characteristics of the noise to provide information on the mass and size distribution of the dust particles.

II. OBSERVATIONS

Before discussing the observational details of the noise produced by particle impacts on the spacecraft near Saturn it is useful to first review the relevant characteristics of the Voyager plasma wave instrument. The plasma wave experiment uses two antenna elements, each 10 long and 1.3 cm in diameter, mounted in a V configuration, as shown in Fig. 1. The antennas are used as a pair of dipole elements, which means that the instrument responds to the difference in the voltage between the two elements. The voltage signals from the antennas are processed in two ways. First, a 16-channel spectrum analyzer provides absolute intensities in 16 frequency channels from 10 Hz to 56 kHz, and second, a wideband receiver provides waveforms of the received signals over the frequency range from about 50 Hz to 14 kHz. The wideband receiver includes an automatic gain control that maintains an approximately constant output amplitude with a feedback time constant of 0.5 sec. For further information on the plasma wave instrument characteristics, see Scarf and Gurnett (1977).

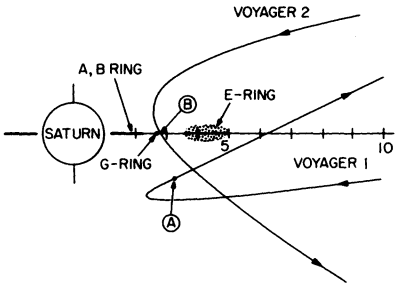

FIG. 2. The Voyager 1 and 2 trajectories plotted in a meridian plane passing through the spacecraft. Voyager 2 crossed the ring plane at 2.88 R_S (R_S = 60,330 km) slightly beyond the G ring and inside the E ring. The E-ring boundaries are not as sharply defined as indicated and the thickness of the E ring has been exaggerated for clarity.

The first evidence of particle impact effects was obtained from Voyager 1, which detected numerous impulsive signals in the wideband data near closest approach (Gurnett *et al.*, 1981). As shown in Fig. 2, the Voyager 1 trajectory crossed through

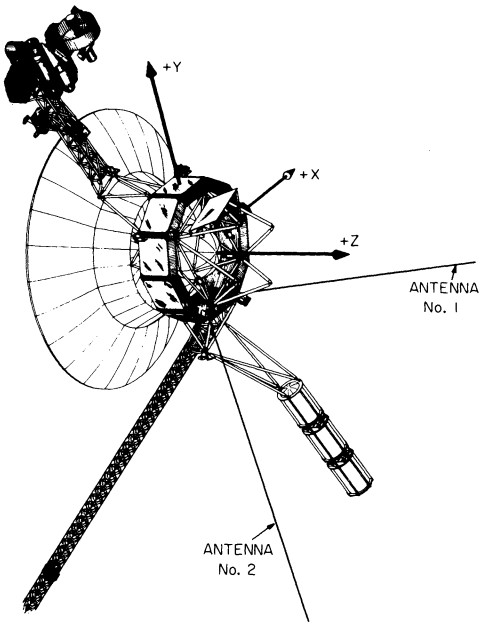

FIG. 1. A sketch of the spacecraft showing the mounting of the two antenna elements and the spacecraft coordinate system used in this analysis. The plasma wave instrument detects the differential voltage between the two antenna elements.

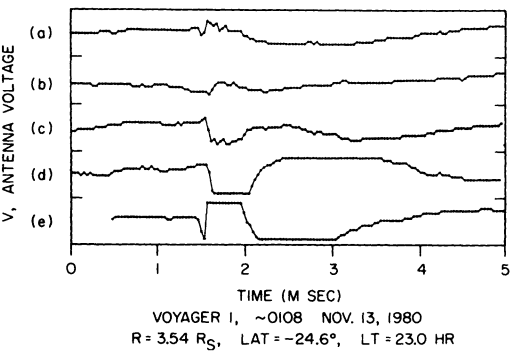

FIG. 3. Representative wideband waveforms of particle impacts detected by Voyager 1 near point A in Fig. 2, well away from the ring plane. The impact rate in this region was relatively low, about four impacts per second.

the ring plane relatively far from the planet, well beyond the E ring, which is the most distant ring that can be detected optically. An example of the wideband waveforms of the impulsive events detected by Voyager 1 is shown in Fig. 3. These impulsive waveforms were obtained at point A in Fig. 2. Typically the impulses consist of an abrupt step, rising at about the time resolution of the wideband channel, which is about 30 μsec, followed by a transient recovery lasting anywhere from 0.5 to several msec. Both positive and negative pulses occur with about equal frequency, consistent with the fact that signals detected by the two antennas are of opposite polarity because of the differential response. Although both Warwick *et al.* (1981) and Scarf *et al.* (1981) suggested that particles hitting the spacecraft could produce impulsive effects, no definitive conclusions were arrived at from the Voyager 1 data concerning the origin of these signals.

A definitive identification of the origin of the impulsive signals detected by Voyager 1 was provided by Voyager 2, which passed through the ring plane much closer to the planet, just beyond the G ring, as shown in Fig. 2. During the few-minute interval around the ring plane crossing, a very intense burst of noise was detected by both the plasma wave and radio astronomy instruments, with the maximum intensity centered almost exactly on the ring plane crossing. The electric field intensities obtained from the 16-channel spectrum analyzer are shown in Fig. 4. At peak intensity the root-mean-square voltage difference between the antenna elements, integrated over the entire frequency spectrum, was 0.248 V. This broadband noise voltage is the largest ever encountered by the Voyager plasma wave instrument. The wideband waveform recording obtained at the ring plane crossing shows that the noise consists of many brief impulses occurring at a rate of several hundred per second. Five representative samples of the waveforms of these impulses are shown in Fig. 5. The waveforms are identical in overall

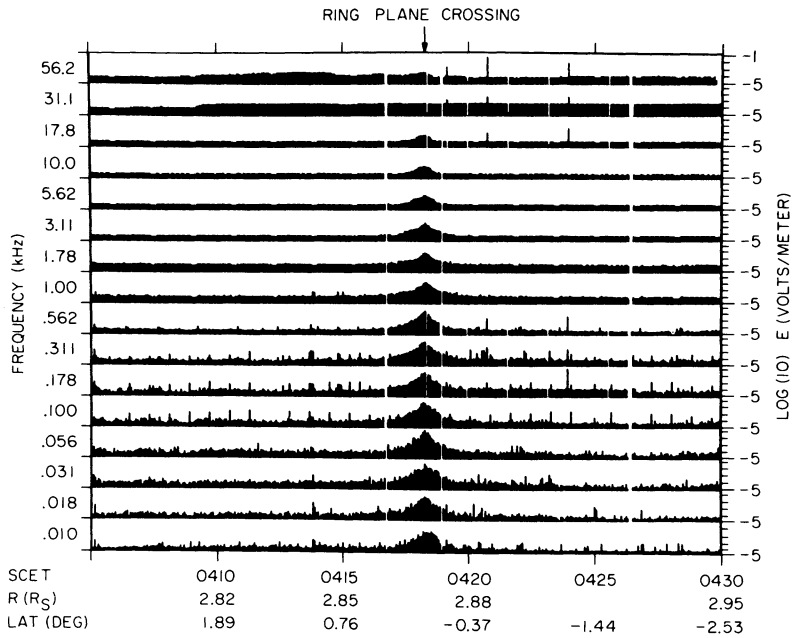

FIG. 4. The electric field intensities from the 16-channel spectrum analyzer during the Voyager 2 ring plane crossing. A very intense broadband burst of noise was detected in a narrow region centered almost exactly on the ring plane crossing.

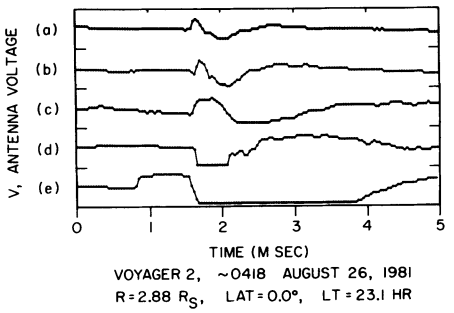

FIG. 5. Representative wideband waveforms of particle impacts detected by Voyager 2 at point B in Fig. 2, coincident with the intense burst of noise at the ring plane crossing. The impact rate at this time was several hundred impacts per second.

characteristics to the waveforms detected by Voyager 1 farther away from the ring plane. The only essential difference is the impulse rate, which is on the order of a few per second for Voyager 1, versus several hundred per second for Voyager 2. Tables I and II summarize all the impulses detected by both Voyagers 1 and 2. As can be seen impulsive signals of the same general type are observed over a large region around Saturn, out to about 35 R_S.

A sound recording of the impacts detected by Voyager 2 at the ring plane crossing has been described by Scarf *et al.* (1982) as sounding like a "hailstorm." The sound recordings of the waveform data give the strong impression that Voyager 2 was being bombarded by many small particles as it passed through the ring plane. The particles must be quite small otherwise there would have been serious damage to the spacecraft. Laboratory tests show, for example, that at a velocity of 14 km/sec a particle of 100 μm radius can penetrate up to 1 mm of aluminum (Frost, 1970), which is comparable to the thickness of some parts of the spacecraft. As far as is known no spacecraft failures have been associated with particle impacts at the ring plane crossing. The particles must therefore have a radius much less than 100 μm.

The wideband measurements all show a very similar and repeatable waveform shape. The waveform usually shows a very rapid rise, with the first peak lasting a few tenths of 1 msec, followed by a somewhat longer second peak of opposite polarity lasting from a large fraction of 1 msec to several milliseconds. The initial rise time of the pulse is almost always on a time scale of about 30 μsec, which corresponds approximatley to the upper cutoff frequency of the wideband receiver. The rise time is therefore probably determined by the instrument response. The radio astronomy instrument shows frequency components extending as high as 10^6 Hz, which suggests that the initial rise time may be as short as a few microseconds. The amplitude of the impulses varies over a wide range, from very small impulses that are barely detectable to very large impulses that severely saturate the receiver. The bottom two waveforms in Fig. 5 illustrate examples where the waveforms are strongly clipped due to receiver saturation effects. Because the automatic gain control continuously adjusts the gain such that an "average" impulse is within the dynamic range of the receiver, only a relatively small fraction, about 10%, are strongly clipped. These strongly clipped waveforms presumably represent impacts by particles that are much larger than "average," but represent only a small fraction of the total distribution. The ratio of the number of negative to the number of positive impulses is about 1.13.

A sequence of frequency spectrums obtained from the wideband data in the vicinity of the ring plane crossing is shown in Fig. 6. The spectrum decreases monotonically with increasing frequency and is remarkably constant in general form throughout the ring plane crossing. At high frequencies, above about 500 Hz, the spectrum varies approximately as f^{-2}, which is the slope expected for a random series of step functions. This part of the spectrum is no doubt produced by the abrupt step at the leading edge of each pulse. It should be noted that the spectrum may be slightly modified by the clipped waveforms. How-

TABLE I

VOYAGER 1, SUMMARY OF WIDEBAND IMPULSE RATE

Date 1980	Time hr min	R_S	λ (deg)	Impulse rate (sec^{-1})	Remarks
Nov. 11	0153	47.1	5.2	—	
	0523	43.7	5.0	—	
	1231	36.8	4.2	0.06	Questionable
	1425	34.9	3.9	—	
	1621	33.1	3.6	—	
	1803	31.5	3.4	—	
	1959	29.5	3.0	—	
Nov. 12	0036	25.0	1.0	0.07	Very weak
	0144	23.9	1.5	1.3	Very weak
	0310	22.5	1.1	0.03	
	0551	19.8	0.0	1.0	
	0635	19.1	−0.3	0.1	
	0849	16.8	−1.5	0.1	
	1001	15.6	−2.3	3.0	
	1257	12.6	−5.0	12.3	
	1830	6.9	−15.8	10.0	
	2107	4.4	−29.3	3.0	
	2252	3.3	−40.3	0.1	High background level
Nov. 13	0109	3.6	−24.2	4.0	
	0326	5.4	−4.4	>10	Rate difficult to estimate
	0730	9.6	9.3	6.6	
	1044	12.9	13.8	—	High background level
	1446	16.9	16.8	0.2	Questionable
	1641	18.9	17.8	—	
	1829	20.7	18.6	0.04	
	2106	23.3	19.4	—	
	2321	25.5	20.0	—	
Nov. 14	0120	27.5	20.4	—	
	0306	29.2	20.8	—	
	0541	31.7	21.3	—	
	1611	41.8	22.5	—	
	0121	49.6	23.1	—	
	0422	53.4	23.3	—	

ever, because the number of clipped waveforms is relatively small, the modification to the spectrum is not believed to be appreciable. A distinct break in the spectrum occurs at a frequency of about 500 Hz, with a tendency toward a flatter spectrum at lower frequencies. The break in the spectrum is caused by the transient recovery part of the waveform, and is not related to the impact rate as was erroneously suggested in the initial reports by Scarf *et al.* (1982) and Warwick *et al.* (1982). It is readily demonstrated that the spectrum of a random series of impulses with a random polarity is independent of the impulse rate. This conclusion can be verified by noting that the break frequency and general shape of the low-frequency part of the spectrum remain essen-

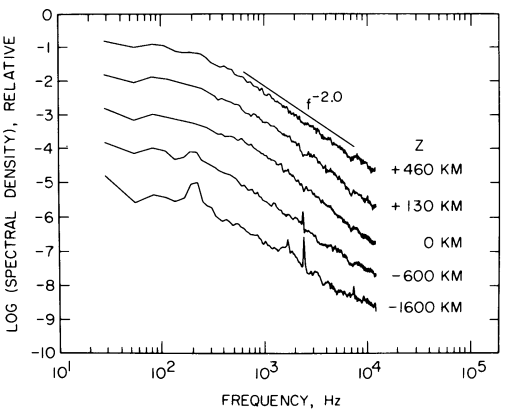

FIG. 6. Selected frequency spectrums of the wideband data at various distances (Z coordinate) from the equator (Voyager 2). Note the close similarity of the spectrum at these widely different positions relative to the equatorial plane.

tially constant throughout the ring plane crossing, even though the impact rate varies by at least an order of magnitude. The constancy of the spectrum indicates that the parameters that control the time scale of the transient response remain essentially unchanged through the entire ring plane crossing.

Because the shape of the spectrum remains constant, the impact noise can be described by essentially two parameters: the impulse rate R and the root-mean-square (rms) voltage V_{rms}. To determine the impulse rate, we developed a computer program that can count the number of impulses in the wideband data. This program looks for two sucessive slopes of the same sign exceeding a preset threshold value. The threshold was adjusted to give good agreement with visual identification of events of the type shown in Figs. 3 and 5. Because the slope criterion often generated false events during the transient recovery phase, particularly for severely clipped waveforms, a dead time t was introduced after each event. The dead time was adjusted to be longer for events with larger slopes, because the receiver usually takes longer to recover after larger events. The average was about 1.6 msec. The true counting rate R was then calculated from the observed counting rate R', using the standard formula for dead time corrections

$$R = \frac{R'}{1 - \bar{t}R'}, \tag{1}$$

where $\bar{t}$ is the average dead time.

The true counting rate, corrected for the dead time using the above procedure, is shown in the top panel of Fig. 7. Because the wideband data were only obtained in a few 48-sec intervals, it was not possible to obtain a continuous determination of the counting rate through the entire ring plane crossing. The regions where the counting rate was actually measured are shown by the solid lines. To make the curve as continuous as possible the counting rate curve has been reflected about the nominal position of the equatorial plane ($Z = 0$). The reflected curve is shown by the dashed lines. Also shown in Fig. 7 is the rms antenna voltage. This voltage was computed from the 16-channel spectrum analyzer by integrating the voltage spectrum over the entire frequency range covered by the plasma wave instrument, 10 Hz to 56.2 kHz. The measurements of the antenna voltage are nearly continuous, with one point every 4 sec, which is the cycle time for the 16-channel spectrum analyzer. The single large peak centered on the ring plane crossing is caused by the impact noise. The numerous smaller peaks, at levels below about 5×10^{-3} V, distributed more or less randomly across the plot, are caused by various spacecraft-generated interference effects that cannot be easily removed from the data.

As can be seen from Fig. 7 the general shape of the counting rate and antenna noise voltage curves are quite similar, each having a well-defined peak centered on the ring plane crossing ($Z = 0$). The time of peak intensity is best determined by the antenna voltage curve and is 1418:17 SCET (spacecraft event time) plus or minus 2 sec.

TABLE II

VOYAGER 2, SUMMARY OF WIDEBAND IMPULSE RATE

Date 1981	Time hr min	R_S	λ (deg)	Impulse rate (sec^{-1})	Remarks
Aug. 24	0846	35.3	14.2	2.0	
	1406	31.4	14.7	2.0	
	1729	28.9	15.1	2.0	
	2018	26.8	15.4	2.0	
	2237	25.0	15.8	2.5	
Aug. 25	1145	14.8	19.0	0.02	
	1146	14.8	19.0	—	
	2007	7.8	24.5	0.5	
	2008	7.8	24.5	1.0	
	2324	5.0	28.5	3.0	
	2325	5.0	28.5	3.0	
Aug. 26	0201	3.1	26.8	1.0	High background level
	0306	2.7	17.0	0.05	High background level
	0418	2.9	0.1	310	
	0419	2.9	−0.1	80	
	0421	2.9	−0.6	40	
	0422	2.9	−0.8	27	
	0424	2.9	−1.3	24	
	0425	2.9	−1.4	19	
	0600	3.9	−16.4	4.0	High background level
	0736	5.2	−23.0	3.0	
	0737	5.2	−23.0	3.0	
	0858	6.4	−25.8	2.0	
	1811	14.1	−29.4	0.1	Questionable
	1812	14.1	−29.4	—	
	2251	17.9	−29.5	—	
	2252	17.9	−29.5	0.1	Questionable

The time of peak intensity is very close to the nominal crossing of the ring plane, which occurred at 1418:15.9 ± 1.5 sec according to the navigational data. Although the two curves shown in Fig. 7 have the same general shape, the basic scale of the variations involved are quite different. Whereas the antenna noise voltage varies by nearly three orders of magnitude during the ring plane crossing the counting rate varies by only one order of magnitude. This marked difference in the counting rate and antenna voltage curves indicates that we are not counting all of the particles, because if all of the particles were being counted the antenna voltage squared (total power) should be directly proportional to the counting rate, $V_{rms}^2 \propto R$.

The reason that all of the particles are not being counted is due to the automatic gain control in the wideband receiver. A full understanding of the operation of the wideband waveform receiver is essential to the proper interpretation of the counting rate data. As described earlier, the basic purpose of the automatic gain control is to maintain an essentially constant average output voltage amplitude, so that the output signal will have a suitable dynamic range for the high-rate telemetry system, which

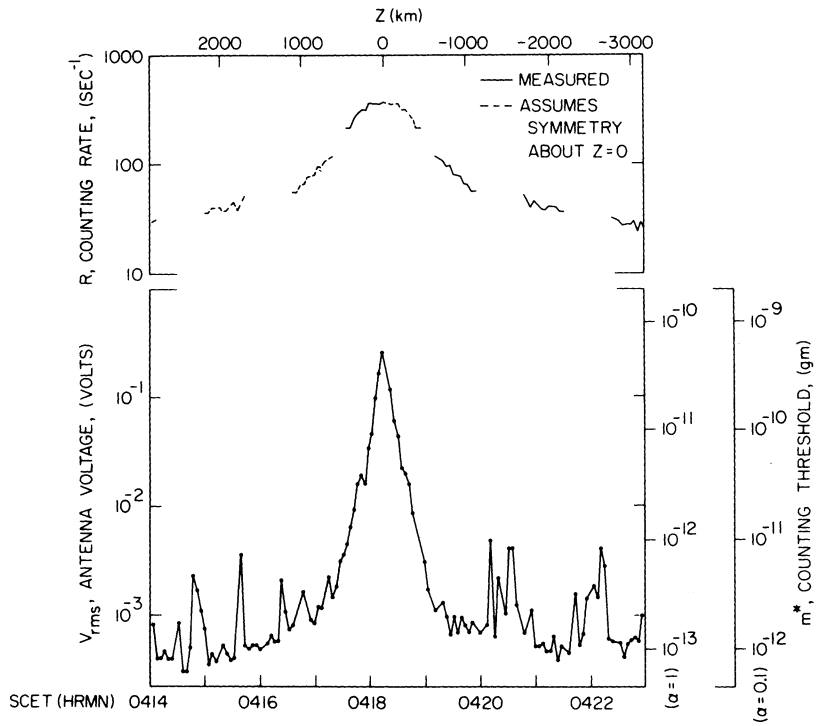

FIG. 7. The counting rate and the rms antenna voltage as a function of time for the Voyager 2 ring plane crossing. The mass m^* is the counting rate threshold estimated for two models ($\alpha = 1$ and $\alpha = 0.1$) that describe the efficiency for collecting charge generated during the impact ionization process. Only particles with masses greater than m^* are counted in the wideband data.

has only 4-bit resolution. To a good approximation the gain of the automatic gain control system is inversely proportional to the rms antenna voltage. Therefore, as the rms noise voltage increases the gain decreases. Because a threshold exists for counting an impulse, the counting threshold increases as the gain decreases, thereby suppressing the counting rate below the true impact rate at the ring plane crossing. For ideal operation of the automatic gain control the counting threshold is directly proportional to the rms antenna voltage. One of our main objectives in the next two sections will be to develop the rationale and techniques for inverting these curves to derive a size and mass distribution for the impacting particles.

III. ANTENNA COUPLING MECHANISMS

Because the signals detected by the plasma wave instrument are electrical in origin some mechanism is needed to convert the mechanical energy of a dust particle impact into an electrical signal. Three mechanisms have been considered: (1) microphonics, (2) direct detection of the charge of a particle hitting the antenna, and (3) detection of charge released by impact ionization.

Microphonics is a general term describing the sensitivity of electrical systems to mechanical vibrations. Mechanical vibrations can produce electrical signals in a variety of ways. For example, a voltage is induced on a charged capacitor if the plate separation is varied, and a voltage is induced in a loop of wire if the area of the loop is changed in the presence of a magnetic field. For the Voyager plasma wave instrument the principal microphonic element is probably the antenna, which can

vibrate and induce voltages because of the changing capacitance. In fact, some microphonic effects are detected. For example, when the low-energy-charged-particle (LECP) instrument is rotated mechanically, and when the tape recorder is being operated, interference signals are detected by the plasma wave instrument. These microphonic effects are, however, totally different from the impulsive signals detected at the ring plane crossing. Usually the microphonic effects can be identified by a pronounced "ringing" response, at frequencies characteristic of the mechanical resonances of the spacecraft structure, which are usually in the range of a few hundred hertz. No structural resonance effects whatever are detectable in the high-resolution spectrum of the ring plane noise, as shown in Fig. 6.

The second possibility considered is that the plasma wave receiver is directly detecting the charge of a dust particle that hits the spacecraft. In a hot plasma dust particles are expected to be charged negatively to a voltage on the order of the plasma thermal energy, $\Phi \simeq \kappa T/e$, which is estimated to be about 10 eV in the vicinity of the ring plane (Bridge *et al.*, 1982). In the presence of uv radiation from the Sun a similar charging effect, but of opposite sign, occurs because of photoelectron emission. In this case the characteristic equilibrium potential is determined by the uv spectrum, and again is about 10 eV. The exact process that is dominant is determined by the electron density, which unfortunately is not very well known in the vicinity of the ring plane. In either case, the potential is expected to be 10 eV or less. The charge on the dust particle can then be calculated from the Coulomb potential which gives

$$Q = (4\pi\epsilon_0 r)\Phi, \qquad (2)$$

where r is the radius of the particle, which is assumed to be spherical. If we consider a relatively large particle of radius $r = 10$ μm the charge works out to be $Q = 1.1 \times 10^{-14}$ C. If such a charged particle hits one of the antenna elements the voltage step produced is $V = Q/C_A$, where $C_A \simeq 90$ pf is the capacity of the antenna (including base capacity). For a particle of 10 μm radius, the corresponding antenna voltage works out to be 1.2×10^{-4} V. This voltage is very small compared to the voltages actually observed. To account for the observed antenna noise levels the particles would have to be charged to voltages much higher than can be accounted for by the observed plasma temperatures. As we will shortly demonstrate, impact ionization is a much more effective source of charge.

The third mechanism to be considered is impact ionization. When a high-velocity projectile, traveling at speeds of many kilometers per second, strikes a solid object the kinetic energy is converted into heat which vaporizes both the projectile and part of the target material. Because of the high temperatures involved, part of the material is also ionized (Drapatz and Michel, 1974). The strong pressure gradient forces then cause the vaporized material to expand, forming a highly compressed gas cloud that expands more or less radially outward from the impact point, as illustrated in Fig. 8. Initially the gas cloud is collision dominated. However, as the density of the expanding cloud decreases a point is reached where collisions are no longer important. At this point recombination ceases and whatever residual ionization is present escapes as an expanding cloud of plasma. The expansion of the plasma cloud is controlled by the self-consistent electric and magnetic field forces present in the plasma. Rough estimates show that the plasma cloud produced by a 10-μm particle reaches the density of the ambient plasma, which is estimated to be about 100 cm^{-3} (Bridge *et al.*, 1982), when the cloud reaches a radius of about 1 m. After this point the charges respond mainly to the sheath fields that exist in the plasma around the spacecraft.

The amount of charge released by a high-velocity impact has been studied by several investigators (Friichtenicht, 1964; Auer and

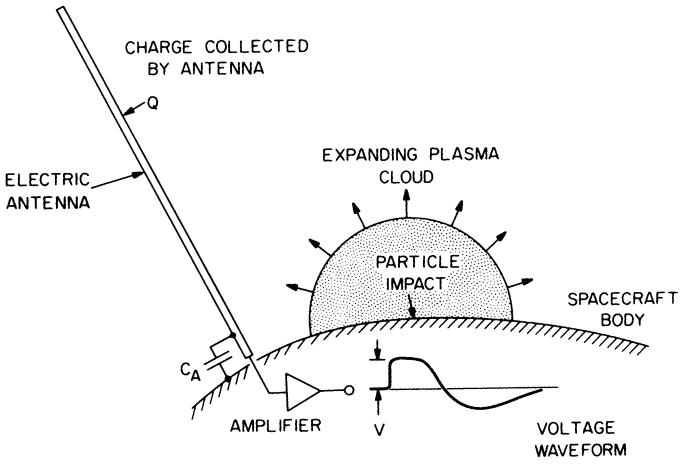

FIG. 8. A schematic illustration of the plasma cloud produced by impact ionization, and the resulting collection of charge Q by one of the antenna elements. The antenna voltage is $V = Q/C_A$, where C_A is the capacitance of the antenna.

Sitte, 1968; Adams and Smith, 1971; Dietzel *et al.*, 1973; McDonnell, 1978; Grün, 1981), mainly for application to interplanetary dust detectors. Laboratory experiments show that the charge Q (of both signs) released in the impact is directly proportional to the mass m of the projectile,

$$Q = km, \tag{3}$$

where k is a yield constant that depends on both the speed of the projectile and the composition of the projectile and target. For a speed of 13.8 km/sec, which is the relative velocity between Voyager and a particle in a circular orbit at the ring plane crossing, a typical value for the ionization yield of a dielectric particle (ice) striking a metal surface (aluminum) is about $k = 0.21$ C/g. If we consider a dust particle of radius $r = 10$ μm and density $\rho = 0.92$ g cm^{-3} (water ice) the charge released is $Q = 8.1 \times 10^{-10}$ C. This charge is nearly five orders of magnitude larger than the charge on a dust particle due to plasma or uv charging effects. If all of this charge (of one sign) were collected by the antenna the resulting antenna voltage would be $V = Q/C_A = 9$ V. This voltage is more than adequate to explain the observed noise levels, even if only a small fraction of the charge is collected or if the particles are much smaller than 10 μm. These simple estimates show that impact ionization is by far the most important charging mechanism.

Next, we address the question of whether the impulses detected are primarily due to impacts with the antenna itself or with the spacecraft body. Of course the spacecraft body is a much bigger target, however, it is likely that only a small fraction of the charge released would be collected by the antenna. On the other hand, impacts on the antenna would probably produce a much larger signal, particularly if the antenna has a net bias voltage so that nearly all charges of one sign (electrons, for example) are collected by the antenna. Fortunately, a simple test can be performed to distinguish the relative importance of impacts with the antenna and with the spacecraft body. Because the antennas are in a V configuration, as shown in Fig. 1, the areas of the two elements, projected into the direction of relative motion of the ring plane particles, is somewhat different. In the spacecraft x, y, z coordinate system shown

in Fig. 1 the velocity of the particles is given by $\mathbf{V} = (4.005, 9.996, -8.640)$ km/sec. From this velocity vector it can be seen that more particles will hit antenna number 1 than will hit antenna number 2. The ratio of the projected areas works out to be $A_1/A_2 = 1.82$. Assuming that all impacts generate voltages of the same polarity, the numbers of positive and negative impulses should occur in a ratio of 1 to 1.82. The observed ratio is 1.13 ± 0.01. The observed ratio is therefore not consistent with detection of impacts only with the antenna. For impacts on the spacecraft body the polarity of the impulse is probably determined by the location of the impact with respect to the y–z symmetry plane of the antenna system. Impacts on the $+x$ side of the y–z plane would tend to produce impulses with a polarity determined by the antenna nearest to that side (antenna no. 1), and impacts on the other side would tend to produce impulses of the opposite polarity (antenna no. 2). The 13% asymmetry in the observed number of positive and negative impulses could be due to either a small asymmetrical contribution from hits on the antenna or to a slight asymmetry in the impact rate on the two sides of the spacecraft. The angle of arrival of the particles relative to the y–z symmetry plane is 16.9°, which may be sufficient to account for the observed asymmetry.

Finally, we consider the mechanisms by which the charge released is coupled to the electric antenna. This is a difficult question to which we do not have a completely satisfactory answer. The problem is difficult for two reasons. First, because the dominate impacts are with the spacecraft body, a full understanding has to take into account the complex geometry of the spacecraft body, which is obviously very difficult. Second, because of the very low plasma temperature at the ring plane crossing a very crucial parameter, namely, the spacecraft potential, is not known. About all that can be said of the spacecraft potential is that it is within plus or minus a few volts of the plasma potential (Bridge *et al.*, 1982). Because the energy of the charged particles emitted in the impact is only a few electron volts (Grün, 1981), a spacecraft potential of only a few volts has a major effect on the trajectory of the emitted particles. The most important parameter is the sign of the potential. Our impression is that the antennas are probably charged positively with respect to the plasma and/or the spacecraft. In this case the electrons are attracted by the antennas. One reason for this conclusion is the rise time of the voltage pulse detected on the antenna, which is on the order of a few microseconds or less. For a temperature of a few electron volts it is readily verified that only electrons have speeds sufficiently high to reach the antenna from the spacecraft on time scales this short. Typical transit times for heavy ions (H^+ and O^+, for example) are a fraction of a millisecond to several milliseconds. A second reason is that the impulse waveforms observed at the ring plane crossing (Fig. 5) are essentially identical to those observed well away from the ring (Fig. 3), where the spacecraft potential is known to be positive with respect to the plasma potential. Because the charge coupling process appears to be the same in the two regions, it seems likely that the spacecraft potential has the same sign in both regions. It should be pointed out that the ring plane crossing is somewhat unusual in that it occurred shortly after the spacecraft passed into the shadow behind Saturn. Under these conditions the spacecraft would normally be expected to charge negative because of the absence of uv photoelectron emission. It is possible, however, that the reflected uv flux from Saturn or the rings may be sufficient to maintain a positive potential (J. Scudder, personal communication).

To take into account the uncertainty in the amount of charge collected by the antenna, we introduce a parameter α, which is the ratio of the charge collected by the antenna to the total charge released. The voltage produced on the antenna is then

$$V = \left(\frac{\alpha k}{C_A}\right) m. \qquad (4)$$

To the extent that the exact coupling problem has not been completely solved, α can be regarded as an adjustable parameter. Some reasonable limits can, however, be placed on α. An obvious upper limit is $\alpha_{max} = 1$. A lower limit can be placed on α based on the following argument. If the collection coefficient for charge emitted by the spacecraft is too small then direct hits on the antenna would start to dominate the response, because presumably the collection coefficient for impacts on the antenna itself is close to one. An estimate of the lower limit on the collection coefficient can be obtained by assuming that the asymmetry in the positive and negative impulse rates is entirely due to the asymmetry in the effective areas of the two antennas (thereby neglecting any contribution due to the asymmetry of the impacts on the spacecraft). If we define R_s and R_A to be the counting rates from impacts on the spacecraft and antenna, the ratio of the negative to positive impulse rate (observed to be 1.13) can be written

$$\frac{R_s^- + R_A^-}{R_s^+ + R_A^+} = 1.13, \qquad (5a)$$

where the (+) and (−) signs refer to positive and negative impulses. To provide an initial estimate of the minimum collection coefficient we assume that the counting rate is proportional to the products of the collection coefficient α, the yield constant k, and the area A, so that $R \propto \alpha k A$. Noting that $R_s^+ = R_s^-$ and $\alpha_A = 1$, Eq. (5a) can then be written

$$\frac{\alpha_s k_s \frac{A_s}{2} + k_A A_{A1}}{\alpha_s k_s \frac{A_s}{2} + k_A A_{A2}} = 1.13, \qquad (5b)$$

where A_s, A_{A1}, and A_{A2} are the effective areas of the spacecraft, antenna number 1 and antenna number 2, and k_s and k_A are the yield constants of the spacecraft and antenna, respectively.

TABLE III

Surface	Material	k (C/g)	Projected area (cm^2)
Antenna No. 1	Be–Cu	0.21	1,126
Antenna No. 2	Be–Cu	0.21	619
Spacecraft body	Al	0.21	10,300
RTG shield	Steel	0.40	2,100
Record	Gold	1.2	212
RTG	Iron–titanate	0.15	4,000

To determine these parameters we surveyed the entire spacecraft and tabulated the yield constants and effective areas for the various types of surfaces on the spacecraft. These values are listed in Table III. Note that the table does not include various painted surfaces and epoxy structures that have very low yield constants. The effective areas, projected into the direction of particle motion, are $A_s = 1.66 \times 10^4$ and $A_A = 1.75 \times 10^3$ cm^2, and the average yield constants are $k_s = 0.23$ and $k_A = 0.21$ C/g. Using these parameters the lower limit for the collection coefficient obtained by solving Eq. (5b) is $\alpha_s = 0.43$. This estimate of the minimum collection coefficient depends somewhat on the mass distribution of the impacting particles (via the assumption that R be proportional to αk). This assumption corresponds to an integral mass distribution varying as m^{-1}. As will be shown in the next section the integral mass distribution probably varies as m^{-2}. In this case the minimum collection coefficient is even larger, $\alpha_s \simeq 0.66$. These estimates show that the antenna is a relatively efficient collector of the electrons emitted by particle impacts on the spacecraft.

IV. MASS AND SIZE DISTRIBUTION

Having considered the possible mechanisms by which particle impacts can produce voltage impulses on the electric antenna, we next describe a method of obtaining the mass and size distribution of the impacting particles from the observed characteristics of the impact noise. Our ba-

sic assumption is that the amplitude of the voltage step produced by the impact is directly proportional to the mass of the particle, as given by Eq. (4). The approach used is based on two characteristics of the impact noise: the counting rate R and the rms antenna voltage $V_{\rm rms}$. To obtain a closed solution it is necessary to make an assumption about the dependence of the mass distribution on distance Z from the equatorial plane. We will make the simplest possible assumption, namely, that mass distribution is independent of Z. This assumption may not be entirely correct, however, in the absence of specific evidence to the contrary, it is the simplest and most reasonable model to give a first estimate of the mass distribution function. The only evidence indicating that the mass distribution is independent of Z is the shape of the noise spectrum in Fig. 6, which, as pointed out earlier, is nearly independent of Z. If the mass distribution varied strongly with Z it seems likely that the change in the average size of the particles would affect the transient response to some extent, hence the shape of the spectrum. Because no change is observed in the spectrum, it seems likely that the mass distribution is constant.

To determine the properties of the impacting particles we must relate the mass distribution to the impact rate and the antenna voltage. For this purpose it is useful to define a mass distribution function $n_{\rm m}$ by the equation

$$dn = n_{\rm m}\,dm, \tag{6}$$

where dn is the number of particles per unit volume in mass range dm. It is convenient to separate the mass distribution function into a number density parameter n_0 and a mass-dependent term, $n_{\rm m} = n_0 g(m)$, where the function $g(m)$ is normalized such that $\int_0^\infty g(m)dm = 1$. Using these definitions it is easy to show that the impact rate is given by the integral

$$R = UA\, n_0 \int_{m^*}^\infty g(m)dm, \tag{7}$$

where U is the speed of the particles, A is the area of the target normal to the direction of incidence, and m^* is the mass threshold for counting particles. If $m^* = 0$ the impact rate is essentially given by the zeroth moment of the mass distribution.

To compute the rms antenna voltage averaged over time T we assume that the impulses consist of rectangular pulses of amplitude V_n and duration τ_n. Using Equation (4) the rms voltage is given by

$$V_{\rm rms}^2 = \frac{1}{T}\sum_n V_n^2\tau_n = \left(\frac{ak}{C_{\rm A}}\right)^2 \frac{1}{T}\Sigma m_n^2\tau_n. \tag{8}$$

Although the duration of the impulses does vary somewhat, these variations are small compared to the variations in the amplitude. The pulse duration is therefore taken to be a constant $\tau_n = \tau$. The discrete summation can be converted to an integral by making use of the relations

$$\frac{1}{T}\sum_n m_n^2 = \int_0^\infty m^2 dR = UAn_0 \int_0^\infty m^2 g(m)dm, \tag{9}$$

which when combined with Eq. (8) give

$$V_{\rm rms}^2 = \tau UAn_0 \left(\frac{\alpha k}{C_{\rm A}}\right)^2 \int_0^\infty m^2 g(m)dm. \tag{10}$$

The rms antenna voltage is seen to be proportional to the second moment of the mass distribution.

In order to solve Eqs. (7) and (10) for the mass distribution function it is convenient to define a new function

$$f(m^*) = R/V_{\rm rms}^2, \tag{11}$$

which is the ratio of the counting rate to the rms voltage squared. As can be seen by taking the ratios of Eqs. (7) and (10), this function is independent of the particle density n_0, and is only a function of the shape of the mass distribution function. Because $f(m^*)$ is independent of the density, this function can be determined from the plot of $R/V_{\rm rms}^2$ versus m^*, provided we assume that the shape of $g(m)$ does not change as the spacecraft passes through the ring plane [i.e.,

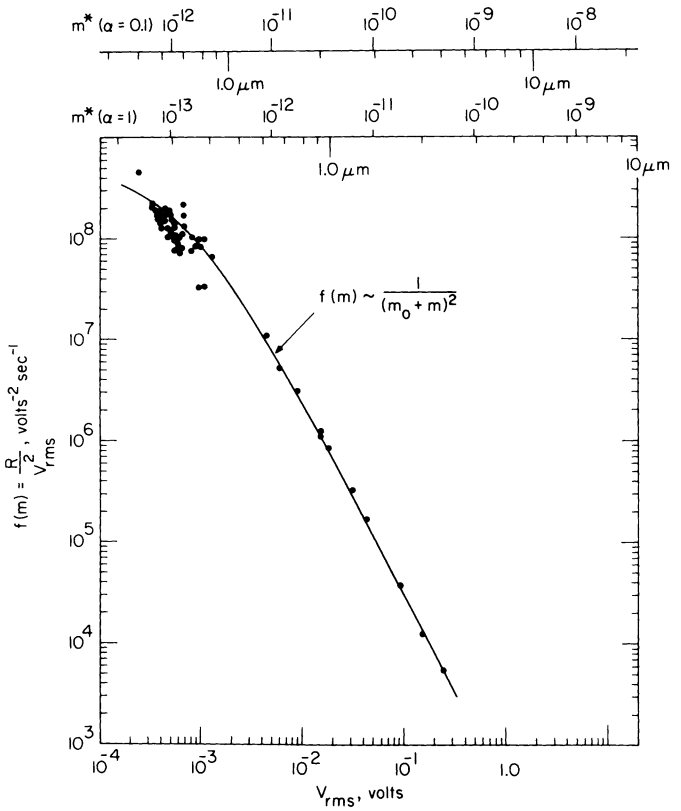

FIG. 9. A plot of the function $f(m)$ as a function of the rms antenna voltage. The conversion of the antenna voltage to particle mass is shown at the top for two values of the collection coefficient ($\alpha = 1$ and $\alpha = 0.1$).

$g(m)$ must be independent of Z]. A plot of $f(m^*)$ is shown in Fig. 9. Because R in $f(m^*)$ depends on the integral of the mass distribution function, this function can be obtained by differentiating $f(m^*)$ with the result

$$n_m = -\frac{V_{rms}^2}{UA}\frac{df}{dm^*}. \qquad (12)$$

It is interesting to note that if we integrate Eq. (12) over all masses, it can be shown that the particle number density parameter is directly proportional to $f(m^*)$ evaluated at $m^* = 0$:

$$n_0 = \frac{V_{rms}^2}{UA} f(m^* = 0).$$

In this case the number density is determined completely independent of the details of the coupling process. The catch is that $f(m^*)$ must be determined at zero threshold ($m^* = 0$), which of course we do not have. In practice the number of particles below the lowest counting threshold simply cannot be determined.

All that remains to complete the solution is to use Eq. (4) to relate the threshold mass to a threshold voltage, which can be written

$$V^* = \left(\frac{\alpha k}{C_A}\right) m^*. \qquad (13)$$

Because of the automatic gain control in the wideband receiver, the threshold voltage for counting impacts is related to the rms voltage by a constant factor, $V^* = \beta V_{rms}$. The constant β can be estimated from

the average shape of the waveform and is approximately $\beta = 0.51$. Combining all of these factors, the threshold mass is related to the rms antenna voltage by

$$m^* = \left(\frac{\beta C_A}{\alpha k}\right) V_{\text{rms}}. \tag{14}$$

This scaling relation can then be used to eliminate m^* in Eq. (12), giving the mass distribution function directly in terms of measured quantities,

$$n_m = -\left(\frac{\alpha k}{\beta C_A}\right) \frac{V_{\text{rms}}^2\, df}{UA\, dV_{\text{rms}}}. \tag{15}$$

For the nominal parameters, $k = 0.23$ C/g, $\beta = 0.51$, and $C_A = 90$ pf, and using $\alpha = 1$, the scale factor in Eq. (14) is 1.99×10^{-10} g/V. This scale factor was used to calculate the mass scales shown on the bottom right side of Fig. 7 and the top of Fig. 9. Two values for the collection coefficient are shown ($\alpha = 1$ and $\alpha = 0.1$) because of the uncertainty in this parameter. Based on the estimates given in the previous section, the collection coefficient is probably in the vicinity of $\alpha \simeq 0.6$.

Equation (15) is most easily evaluated by fitting a function to the data points in the plot of $f(m^*)$ in Fig. 9. For voltages above 10^{-2} V the function $f(m^*)$ varies almost exactly as m^{-2}, which means that $g(m)$ varies as m^{-3} in this range. At low voltages, below 10^{-2} V, a distinct break occurs in the slope of the function. A very good fit can be obtained at all voltages by using a function of the form

$$f(m^*) \sim \frac{1}{(m_0 + m^*)^2}. \tag{16}$$

The constant m_0 determines the break point in the function. For $\alpha = 1$ the break occurs at $m_0 = 1.44 \times 10^{-13}$ g and for $\alpha = 0.1$ it occurs at $m_0 = 1.44 \times 10^{-12}$ g. Because the measurements that determine the break point all occur at very low voltages, where substantial errors may be present, the exact position of the break point must be considered somewhat uncertain.

Using the functional form for $f(m^*)$ given in Eq. (16) it can be shown using Eq. (15) that the mass distribution is of the form

$$n_m = n_0 \frac{2m_0^2}{(m + m_0)^3}, \tag{17}$$

where the term $2m_0^2$ provides the proper normalizing constant such that $\int_0^\infty g dm = 1$. The best-fit mass distribution function is shown in Figs. 10 and 11 at a variety of Z values using $\alpha = 1$ and $\alpha = 0.1$, respectively. Note that because the number density term n_0 is proportional to V_{rms}^2 [see Eq. (15)], the density distribution is very sharply peaked near the equatorial plane, much more so than might be expected from the plot of R versus Z in Fig. 7. The reason for this effect is that the wideband receiver is counting only a small fraction of the particles near the equator because the gain is set very low in this region. The approximate threshold for counting impacts with the wideband receiver is indicated on the distribution function plots in Figs. 10 and 11. Only particles with masses above these thresholds are counted with the wideband system. The effective north–south thickness of the particle distribution, defined by $n_0(\max) L_z = \int n_0 dz$, can be computed from the distribution function and is approximately $L_z = 106$ km. This effective thickness is much smaller than the thickness of approximately 1000 km given in the initial reports by Scarf *et al.* (1982) and Warwick *et al.* (1982). This difference is attributed to the definition of the thickness, which in the cases of Scarf *et al.* and Warwick *et al.* was taken to be the region over which a substantial number of particles could be detected. In our case the effective thickness is the distance which when multiplied by the peak density gives the total number of particles per unit area. Also, as discussed above, the counting rate curve tends to give an exaggerated impression of the north–south thickness.

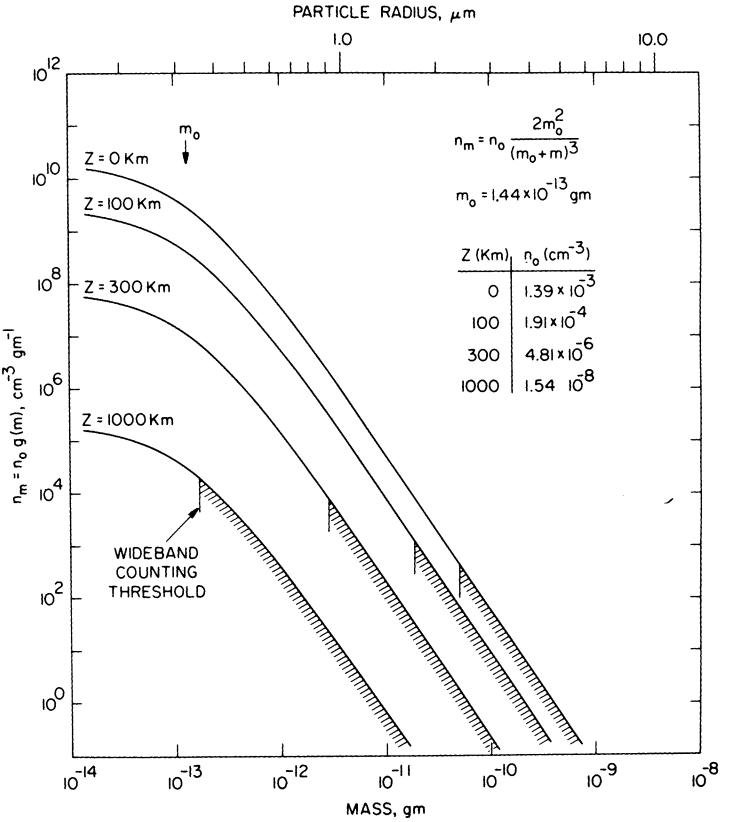

FIG. 10. The best-fit mass distribution function for the $\alpha = 1$ model as a function of distance Z from the equatorial plane. Only particles with masses above the wideband counting threshold are counted by the wideband receiver.

V. DISCUSSION AND CONCLUSION

The observations of particle impacts on the Voyager 2 spacecraft by the plasma wave instrument were described and analyzed. A strong case was presented indicating that the plasma wave instrument detected charges released by impact ionization of small micron-sized particles striking the spacecraft. Most of the impacts detected were caused by particles hitting the spacecraft body. The analysis is complicated by the fact that the coupling of the impact ionization to the electric antenna is poorly understood, both because of the uncertainty in the equilibrium potential of the spacecraft and because of the complicated geometric boundary conditions involved. The basic assumption used in the analysis is that the voltage impulse detected is proportional to the mass of the colliding particle. Based on laboratory investigations of particle impact ionization effects this appears to be a very reasonable assumption. The primary uncertainty has to do with the coupling of the charge released to the electric antenna. To take into account the uncertainties involved, the coupling was represented by a collection coefficient that represents the fraction of the charge collected by the antenna. On relatively crude grounds it is estimated that the collection coefficient is somewhere in the range from 0.1 to 1 with a nominal value of 0.6. Even with these un-

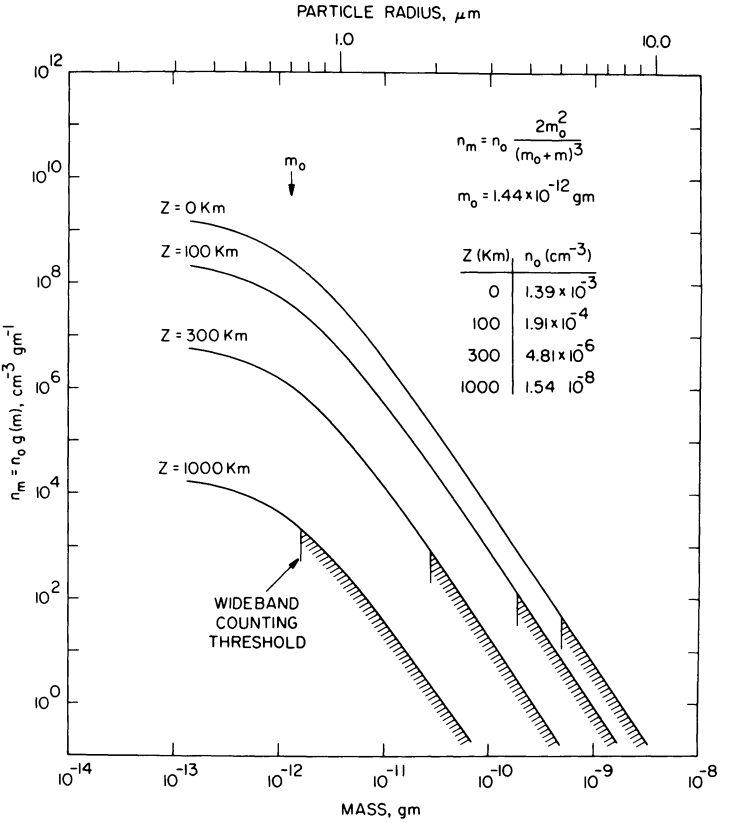

FIG. 11. The best-fit mass distribution function for the $\alpha = 0.1$ model.

certainties, the particle sizes involved can be confidently estimated to be in the range of 1 μm. If one makes the further, seemingly reasonable assumption that the size distribution does not depend on the distance from the equatorial plane, a complete solution can be obtained for the mass distribution function as a function of distance from the equatorial plane. The results indicate that the mass distribution function varies as m^{-3}, with a decreasing slope for masses less than about 10^{-13} to 10^{-14} g. The effective north–south thickness of the particle distribution near the equatorial plane is 106 km.

As indicated in Fig. 2, the Voyager 2 ring plane crossing occurred slightly outside of the G ring. Because of the close proximity to the G ring it seems likely that the particles detected at the ring plane crossing are associated with this ring. Although the G ring was clearly visible in the Voyager 2 images, no scattered light could be detected at the radius where Voyager 2 crossed the ring plane (Smith *et al.*, 1982). From the imaging data an upper limit to the optical depth τ normal to the ring plane can be obtained at this radial distance. The upper limit is estimated to be about 10^{-6} (R. Terrile, personal communication). The optical depth in the central part of the G ring is about 10^{-4} (Smith *et al.*, 1982). The width of the G ring could not be reliably determined due to smearing of the image. The optical depth determined from the imaging can be compared to the optical depth computed from the mass distribution function. To make this comparison we first compute the optical depth considering only the geometrical cross section of the particles, neglect-

ing for the moment any angular or wavelength dependences in the scattering. For spherical particles the cross-sectional area varies as the two-thirds power of the mass, $A = A_0(m/m_0)^{2/3}$. The optical depth for an optically thin medium is then given by the integral

$$\tau = n_0(\max) L_z A_0 \int_0^\infty \left(\frac{m}{m_0}\right)^{2/3} \frac{2m_0^2}{(m_0 + m)^3}\, dm, \quad (18)$$

where A_0 is the cross-sectional area of a particle of mass m_0. For a collection coefficient of $\alpha = 1$ the break point mass m_0 is 1.44×10^{-13} g, which corresponds to a radius $r_0 = 0.334$ μm and an area $A_0 = 3.51 \times 10^{-9}$ cm^2, assuming H_2O ice. Using the nominal parameters developed in the $\alpha = 1$ model ($n_0 = 1.39 \times 10^{-3}$ cm^{-3} and $L_z = 106$ km) the optical depth works out to be $\tau = 4.18 \times 10^{-5}$. For the $\alpha = 0.1$ model the optical depth is increased by a factor of 4.64.

The computed optical depths are much less than one, indicating an optically thin medium, as expected. The optical depth computed from the mass distribution function is larger than the imaging value of 10^{-6} estimated for the ring plane crossing, but less than the imaging value of 10^{-4} for the central region of the G ring. Thus the optical depth computed from the measured mass distribution function is in a plausible range. The discrepancy with the imaging value at the ring plane crossing could be accounted for by several factors. First, as can be seen from Eq. (18), the main contribution to the optical depth comes from particles of low mass, near m_0, where the greatest uncertainties occur in the measurements. The portion of the spectrum that is most accurately determined, at $m \gg m_0$, makes only a minor contribution to the optical depth. Thus minor errors in the shape of the spectrum at low masses could significantly modify the optical depth. Second, as discussed earlier, both the yield constant k and the collection coefficient α have substantial uncertainties. Both of these factors directly affect the estimated mass and size of the particles [see Eq. (13)]. Because the yield constant was not available for H_2O ice particles and had to be estimated from other materials, the factor k could easily be in error by up to a factor of 3 or more. Note that the best agreement with the optical data is obtained for a collection coefficient of $\alpha = 1$. If the collection coefficient were much smaller than one, for example, 10^{-2} or 10^{-3}, the computed optical depth would be unacceptably large. Thus the comparison with the optical measurements supports our earlier conclusions that the collection coefficient must be rather large, not substantially less than one. Third, as can be seen from Figs. 10 and 11, most of the particles have diameters less than 1 μm, comparable to or less than the wavelength of light. The angular distribution of optical scattering in this size range is known to be anisotropic, with a strong peak in the forward direction (Van de Hulst, 1957). This anisotropy has the effect of reducing the optical depth computed from the measured mass distribution. Unfortunately, the angular distribution of scattering is not very well known for the G ring particles, so it is difficult to accurately estimate the correction due to this effect. Fourth, it is possible that regions of the G ring imaged by Voyager were not representative of the region where the spacecraft actually passed through the ring plane. For example, any slight eccentricity in the ring or fine structure, such as has been observed in the F ring (Lane *et al.*, 1982), could mean that the spacecraft passed through a region of higher particle concentrations than would be indicated by the imaging data.

Finally, the mass distribution function derived in this study can be compared with the charged particle absorption signatures reported by Van Allen *et al.* (1980) near the G ring. The crucial quantity for comparison with energetic proton absorption is the mass density per unit area normal to the

ring plane. This quantity is given by the integral

$$\lambda = n_0(\max) L_z \int_0^\infty m \frac{2m_0^2}{(m_0 + m)^3} dm. \quad (19)$$

Again using the nominal parameters derived for the $\alpha = 1$ model, the mass per unit area works out to be $\lambda = 7.07 \times 10^{-10}$ g cm^{-2}. For the $\alpha = 0.1$ model, the mass per unit area increases by a factor of 10. Based on recent estimates by Van Allen (personal communication), these values are at least an order of magnitude smaller than the mass per unit area required to account for the G ring absorption feature, and are not large enough to cause a detectable absorption effect at the radius of the Voyager 2 ring plane crossing. The mass distribution function derived in this study therefore appears to be in an acceptable range relative to the limits imposed by charged particle absorption effects.

ACKNOWLEDGMENTS

The authors would like to thank R. Terrile of the Jet Propulsion Laboratory and J. A. Van Allen for their helpful comments on the interpretation of these data. The research at the University of Iowa was supported by NASA through Contract 954013 with JPL, through Grants NGL-16-001-002 and NGL-16-001-043 with NASA Headquarters, and by the Office of Naval Research. The research at TRW was supported by NASA through Contract 954012 with JPL.

REFERENCES

ADAMS, N. G., AND D. SMITH (1971). Studies of micro particle impact phenomena leading to the development of a highly sensitive micrometeoroid detector. *Planet. Space Sci.* **19,** 195.

AUER, S., AND K. SITTE (1968). Detection technique for micrometeoroids using impact ionization. *Earth Planet. Sci. Lett.* **4,** 178.

BRIDGE, H. S., F. BAGENAL, J. W. BELCHER, A. J. LAZARUS, R. L. MCNUTT, J. D. SULLIVAN, P. R. GAZIS, R. E. HARTLE, K. W. OGILVIE, J. D. SCUDDER, E. C. SITTLER, A. EVIATAR, G. L. SISCOE, C. K. GOERTZ, AND V. M. VASYLIUNAS (1982). Plasma observations near Saturn: Initial results from Voyager 1. *Science* **215,** 563.

DIETZEL, H., G. EICHHORN, H. FECHTIG, E. GRÜN, H. J. HOFFMAN, AND J. KISSEL (1973). The HEOS 2 and Helios micrometeoroid experiments. *J. Phys. E: Sci. Instrum.* **6,** 209.

DRAPATZ, S., AND K. W. MICHEL (1974). Theory of shock wave ionization upon high velocity impact of micrometeorites. *Z. Naturforsch. A* **29,** 870.

FRIICHTENICHT, J. F. (1964). Micrometeoroid simulation using nuclear acceleration techniques. *Nucl. Instrum. Methods* **28,** 70.

FROST, V. C. (1970). Meteoroid damage assessment. *NASA Spec. Publ.* **8042,** 30.

GRÜN, E. (1981). Experimental studies of impact ionization. *ESA Rep. (Paris)* **SP-155,** 81.

GURNETT, D. A., W. S. KURTH, AND F. L. SCARF (1981). Plasma waves near Saturn: Initial results from Voyager 1. *Science* **212,** 235.

LANE, A. L., C. W. HORD, R. A. WEST, L. W. ESPOSITO, D. L. COFFEEN, M. SATO, K. E. SIMMONS, R. B. POMPHREY, AND R. B. MORRIS (1982). Photopolarimetry from Voyager 2: Preliminary Results on Saturn, Titan, and the Rings. *Science* **215,** 537.

MCDONNELL, J. A. M. (1978). Microparticle studies by space instrumentation. In *Cosmic Dust* (J. A. M. McDonnell, ed.). Wiley, New York.

SCARF, F. L., AND D. A. GURNETT (1977). A plasma wave investigation for the Voyager mission. *Space Sci. Rev.* **21,** 289.

SCARF, F. L., D. A. GURNETT, AND W. S. KURTH (1981). *A Description of the Signals on Voyager Plasma Wave Tape S-1, "Voyager at Saturn."* TRW Technical Report 23498-6041-UT-00.

SCARF, F. L., D. A. GURNETT, W. S. KURTH, AND R. L. POYNTER (1982). Voyager 2 plasma wave observations at Saturn. *Science* **215,** 287.

SMITH, B. A., L. SODERBLOM, R. BATSON, P. BRIDGES, J. INGE, H. MASURSKY, E. SHOEMAKER, R. BEEBE, J. BOYCE, G. BRIGGS, A. BUNKER, S. A. COLLINS, C. J. HANSEN, T. V. JOHNSON, J. L. MITCHELL, R. J. TERRILE, A. F. COOK II, J. CUZZI, J. B. POLLACK, G. E. DANIELSON, A. P. INGERSOLL, M. E. DAVIS, G. E. HUNT, D. MORRISON, T. OWENS, C. SAGAN, J. VEVERKA, R. STROM, AND V. E. SUOMI (1982). A new look at the Saturn system: The Voyager 2 images. *Science* **215,** 504.

VAN ALLEN, J. A., B. A. RANDALL, AND M. F. THOMSEN (1980). Sources and sinks of energetic electrons and protons in Saturn's magnetosphere. *J. Geophys. Res.* **85,** 5679.

VAN DE HULST, H. C. (1957). *Light Scattering by Small Particles.* Wiley, New York.

WARWICK, J. W., J. B. PEARCE, D. R. EVANS, T. D. CARR, J. J. SCHAUBLE, J. K. ALEXANDER, M. L. KAISER, M. D. DESCH, M. PEDERSEN, A. LECACHEUX, G. DAIGNE, A. BOISCHOT, AND C. H. BARROW (1981). Planetary radio astronomy observations from Voyager 1 near Saturn. *Science* **212,** 239.

WARWICK, J. W., D. R. EVANS, J. H. ROMIG, J. K. ALEXANDER, M. D. DESCH, M. L. KAISER, M. AUBIER, Y. LEBLANC, A. LECACHEUX, AND B. M. PEDERSEN (1982). Planetary radio astronomy observations from Voyager 2 near Saturn. *Science* **215,** 582.